Supplementary Information for "Gate-tunable flat bands in van der Waals patterned dielectric superlattices"

Superlattice band structure

For a 2D trianglular superlattice, we model the Hamiltonian as $\mathcal{H} = \mathcal{H}_0 + V(\mathbf{r})$, with

$$\mathcal{H}_0 = v\hbar(\sigma_x k_x + \xi\sigma_y k_y) + \Delta\sigma_z, \tag{S-1}$$

and

$$V(\mathbf{r}) = V_s\sigma_0 \sum_{j=1}^{3} 2\cos(\mathbf{G}_j\cdot\mathbf{r}),\ \mathbf{G}_j = \frac{4\pi}{3a}\Big(\cos\frac{j\pi}{3}, \sin\frac{j\pi}{3}\Big). \tag{S-2}$$

Here $\mathbf{G}_j$ are the triangular superlattice reciprocal vectors oriented 60° relative to each other. The band structure is obtained by diagonalizing the Bloch Hamiltonian, whose (pq, mn)-th 2×2 block reads

$$\big[H(\mathbf{k})\big]_{pq,mn} = \langle \mathbf{k}_{pq}|\mathcal{H}_0|\mathbf{k}_{mn}\rangle + V_s \sum_{j=1,2,3} \langle \mathbf{k}_{pq}|2\cos(\mathbf{G}_i\cdot\mathbf{r})\sigma_0|\mathbf{k}_{mn}\rangle, \tag{S-3}$$

where $\mathbf{k}_{pq} = \mathbf{k} + p\mathbf{G}_0 + q\mathbf{G}_1$ with $\mathbf{k}$ within the first Brillouin zone, $p, q \in \mathbb{Z}$, and $|\mathbf{k}_{pq}\rangle$ is the plane wave basis. The same applies to $\mathbf{k}_{mn}$ and $|\mathbf{k}_{mn}\rangle$ For any (pq, mn) block, it is coupled to the other 6 blocks: $(pq\pm 1, mn)$, $(pq, mn\pm 1)$, $(pq-1, mn+1)$ and $(pq+1, mn-1)$.

Numerically, we have to truncate the infinitely large matrix $H(\mathbf{k})$ into a finite sized $H_N(\mathbf{k})$ in which $p, q \in [-N, N]$, and $H_N(\mathbf{k})$ has a finite dimension $2(2N+1)^2$. Throughout the paper, we find $N = 4$ (162 mini-bands in total) is sufficient to ensure the dispersion for the mini-bands close to the intrinsic gap converge.

Electric potential from generalized Poisson equation

For a non-uniform dielectric environment, we have the generalized Poisson equation

$$\nabla\cdot\mathbf{D}(\mathbf{r}) = -\nabla\cdot[\epsilon(\mathbf{r})\nabla\phi(\mathbf{r})] = 4\pi\rho_{\text{free}}(\mathbf{r}). \tag{S-4}$$

With the knowledge of $\epsilon(\mathbf{r})$, and the values of $\phi(\mathbf{r})$ at the top and bottom gates, we can solve $\phi(\mathbf{r})$ using Eq. (S-4).

We now investigate the electric potential in the configuration illustrated in the Fig. S-1. In this configuration, there is a single hole in the SiO_2 dielectric substrate, which is in between a top gate and bottom gate. Since we have rotational symmetry in the x-y plane, we choose cylindrical coordinates (ρ, φ, z):

$$x = \rho\cos\varphi, \quad y = \rho\sin\varphi, \quad z = z, \tag{S-5}$$

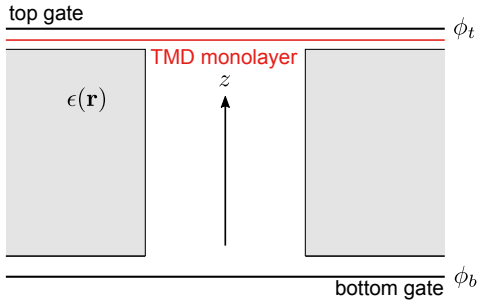

FIG. S-1: The inhomogeneous dielectric environment simulated in Fig. 1b. Gray regions are SiO_2 substrate and the white region denotes an air hole. A TMD monolayer lies in between the substrate and the top gate. Parameters used in the simulation: the distance (exaggerated here for illustration) between the top/bottom gate and the top/bottom of the SiO_2 substrate is 3 nm; the thickness of the SiO_2 substrate in the z-direction is 40 nm; the radius of the air hole within the SiO_2 substrate is 10 nm; $\phi_b - \phi_t = 5$ eV.

expressing $\epsilon(\mathbf{r}) = \epsilon(\rho, z)$, $\phi(\mathbf{r}) = \phi(\rho, z)$. Using rotational symmetry, we eliminate the azimuthal angle to obtain the 2D equation:

$$\frac{1}{\rho}\frac{\partial}{\partial\rho}\left[\rho\ \epsilon(\rho,z)\frac{\partial\phi(\rho,z)}{\partial\rho}\right] + \frac{\partial}{\partial z}\left[\epsilon(\rho,z)\frac{\partial\phi(\rho,z)}{\partial z}\right] = 0. \tag{S-6}$$

To proceed we specify $\epsilon(\rho, z)$ in the whole region ($\epsilon = 4$ for gray regions and $\epsilon = 1$ for white regions), and the boundary conditions at the bottom and top gates for $\phi(\rho, z)$ (see Fig. S-1, electric potentials for top and bottom gates are set to ϕ_t and ϕ_b, respectively). We can numerically solve the $\phi(\rho, z)$ in the whole region. In so doing, we used *Mathematica* NDSolve to solve the differential Eq. S-6.

In our simulation, we obtain $V_s \approx 12.5$ meV when we set $\phi_b - \phi_t = 5$ eV(see Fig. 1b). This correspond to an electric field strength $E \approx 0.11\,\text{V}\,\text{nm}^{-1}$ which is smaller than the breakdown electric field strength ($\sim 0.5\,\text{V}\,\text{nm}^{-1}$) for hBN.

Superlattice-Induced Particle-hole asymmetry

The bare TMD Hamiltonian $\mathcal{H}_0 = v\hbar(\sigma_x k_x + \xi\sigma_y k_y) + \Delta\sigma_z$ has eigen energy $\varepsilon^{\pm}_{\mathbf{k}} = \pm\sqrt{v^2\hbar^2|\mathbf{k}|^2 + \Delta^2}$ and eigen states

$$u^+_{\mathbf{k}} = \begin{bmatrix}\cos(\theta_{\mathbf{k}}/2)e^{-i\phi_{\mathbf{k}}/2}\\ \sin(\theta_{\mathbf{k}}/2)e^{i\phi_{\mathbf{k}}/2}\end{bmatrix}, \quad u^-_{\mathbf{k}} = \begin{bmatrix}\sin(\theta_{\mathbf{k}}/2)e^{-i\phi_{\mathbf{k}}/2}\\ -\cos(\theta_{\mathbf{k}}/2)e^{i\phi_{\mathbf{k}}/2}\end{bmatrix}, \tag{S-7}$$

where $\cos\theta_{\mathbf{k}} = \Delta/\sqrt{v^2\hbar^2|\mathbf{k}|^2 + \Delta^2}$ and $\tan\phi_{\mathbf{k}} = k_y/k_x$. The particle-hole operation $\mathcal{P} = i\sigma_y\mathcal{K}$ ($\mathcal{K}$ is the complex conjugation) transforms $\mathcal{P}u^+_{\mathbf{k}} = u^-_{\mathbf{k}}$, i.e., each eigenstate $u^+_{\mathbf{k}}$ at energy $\varepsilon^+_{\mathbf{k}}$ has a copy $\mathcal{P}u^+_{\mathbf{k}}$ at energy $\varepsilon^-_{\mathbf{k}}$. Meanwhile it also satisfies $\mathcal{P}\mathcal{H}_0\mathcal{P}^{-1} = -\mathcal{H}_0$. Therefore $\mathcal{H}_0$ has a particle-hole symmetry.

However, for the superlattice potential $V(\mathbf{r})$ we have $\mathcal{P}V(\mathbf{r})\mathcal{P}^{-1} = V(\mathbf{r})$. This breaks the particle-hole symmetry for the overall Hamiltonian, i.e., $\mathcal{P}\mathcal{H}\mathcal{P}^{-1} \neq -\mathcal{H}$.

Instead, the hamiltonian $\mathcal{H}$ possesses a different type of symmetry. To see this, we define a composite particle-hole and voltage flip operation $\tilde{\mathcal{P}} = \mathcal{P}\mathcal{M}_z$. Here $\mathcal{P}$ is the particle-hole operation (as defined above), and the mirror operation $\mathcal{M}_z$ flips $V(\mathbf{r}) \to -V(\mathbf{r})$ by interchanging the top and bottom gate potential keeping $\mathcal{H}_0$ intact. Using this composite operation we recover $\tilde{\mathcal{P}}\mathcal{H}\tilde{\mathcal{P}}^{-1} = -\mathcal{H}$. More explicitly, when $V_s \to -V_s$ then $\varepsilon_{\mathbf{k}} \to -\varepsilon_{\mathbf{k}}$ are interchanged.

Including intrinsic bare TMD conduction and valence band mass asymmetry

We note that the bare particle-hole symmetric $\mathcal{H}_0$ that we focus on in the main text is a convenient description that captures the essential low energy physics and band geometry for TMDs. However, real TMD materials can also exhibit asymmetry between the conduction and valence band masses [S1]. This mass difference can be captured in a straightforward fashion by including an additional k-dependent scalar term into $\mathcal{H}_0$ so that $\mathcal{H}_0 \to \hbar^2|k|^2/2m_{\rm asy} + \mathcal{H}_0$. With the extra term $\hbar^2\mathbf{k}^2/2m_{\rm asy}$, $m_c \to m_c/(1 + m_c/m_{\rm asy})$ and $-m_v \to -m_v/(1 - m_v/m_{\rm asy})$. A large and positive $m_{\rm asy}$ makes m_c (m_v) lighter (heavier). The conduction and valence band mass asymmetries for several TMDs are tabulated below, taken from Ref. [S1].

Taking this replacement $\mathcal{H}_0 \to \hbar^2|k|^2/2m_{\rm asy} + \mathcal{H}_0$, we calculated the PDS superlattice miniband structure using the band parameters for WSe_2 in Fig. (S-2) using the same parameters as Fig. 2a in the main text but with conduction and valence band masses that are asymmetric (see caption). We find that the miniband structure (dashed lines) when asymmetric conduction and valence band masses are included are very similar to that obtained for symmetric conduction and valence band masses (solid lines). Importantly, the flat minibands (blue line) remain robust and stay flat and well separated from the adjacent minibands. As a result, we conclude the mass asymmetries found in the TMDs do not qualitatively affect our conclusions in the main text – namely that flat minibands can be obtained using the PDS protocol.

	WSe_2	MoS_2	$MoSe_2$	WS_2
$(m_v - m_c)/m_e$	0.07	0.08	0.03	0.09

TABLE S-I: Effective mass differences between the conduction band and valence band for TMDs; data from Ref. [S1]

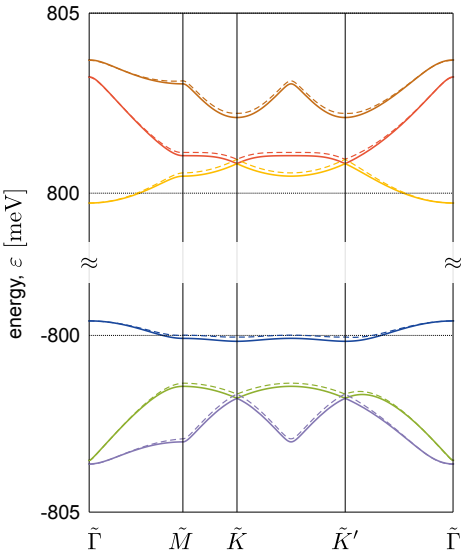

FIG. S-2: PDS miniband dispersion close to the intrinsic band gap without (solid lines) and with (dashed lines) a conduction/valence band mass asymmetry term $\hbar^2|\mathbf{k}|^2/2m_{\rm asy}$ in the bare TMD hamiltonian. Parameters are the same with those in Fig. 2a in the main text, and we used $m_{\rm asy} = 4.46m_e$ so that $m_v - m_c = 0.07m_e$ for WSe_2.

Mini-band Berry curvature distribution, valley Chern number, and miniband gapped-Dirac-cone

The PDS superlattice potential can also modify the winding of the pseudo-spins as well as the miniband quantum geometry. To display this, we plot the Berry curvature distribution in the top most valence mini-band for $V_s > 0$ (see Fig. S-3a) and $V_s < 0$ (see Fig. S-4a). In what follows, we concentrate on the Berry curvature for minibands from the (original) K' valley with $\xi = -1$ (see Eq. 1). We first note that the Berry curvature around a single bare gapped Dirac cone in the valence band of the TMD (when $V_s = 0$) has a positive sign for K' valley, and monotonically decreases in magnitude away from the Dirac point.

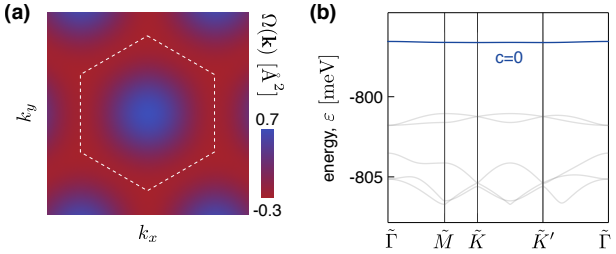

FIG. S-3: (a) Berry curvature distribution for the top most valence miniband. Dashed hexagons denote the mini Brillouin zone. (b) Dispersion for the mini-bands close to the intrinsic band gap, and the valley Chern number for the top most valence miniband. Parameters are the same with those in Fig. 2a in the main text, except that $V_s = 1.5\,$meV.

We now focus on the topmost flat valence miniband when $V_s > 0$. Now the (positive) sign of the Berry curvature from the bare gapped Dirac cone in the TMD is reflected in the center of the MBZ (see Fig. S-3a). However, PDS induced Bragg scattering close to the MBZ boundaries produces a different winding of the pseudospin and a different sign of Berry curvature close to MBZ boundaries. This reconstructs the Berry curvature distribution. As a result, the net Berry flux through the MBZ for the top most valence miniband is $\mathcal{C} = 0$.

Next, we turn to the topmost flat miniband when $V_s < 0$. Similar to the case discussed above, the positive sign of the Berry curvature from the bare gapped Dirac cone in the TMD is again reflected in the center of the MBZ. However, Bragg scattering at MBZ corners in the top valence miniband for $V_s < 0$ is significant and dramatically changes the winding of the pseudo-spinor wavefunction; indeed the Berry curvature distribution is concentrated at the MBZ corners displaying large and negative value (see small white dots). Note that the white dots appear at both $\tilde{K}$ and $\tilde{K}'$ points; their common sign indicates that chirality of the pseudospinors at these points is the same. As a result, within this (blue) band (Fig. S-4b), we obtain a non-vanishing net Berry flux of $\mathcal{C} = -1$ in a single (original) valley (see Fig. S-4).

The large Berry flux in the the top valence blue miniband (for $V_s < 0$) arises from a very small minigap with the adjacent miniband just below it (green). Indeed, when zoomed-in a small minigap between the two top valence minibands of order $\sim \mu$eV appears at the $\tilde{K}'$ point (see Fig. S-4b); a similar gap also appears at $\tilde{K}$ point. We note parenthetically that this small gap is larger than the numerical mesh resolution from our numerical diagonalization routine, allowing us to extract the minigap value shown. Indeed, the lower miniband (green) also displays the same behavior with a sharp distribution of Berry curvature peaked at the $\tilde{K}, \tilde{K}'$ points; these have opposite sign to the blue miniband above it with a concomitant $\mathcal{C} = -1$ in a single valley.

While the finite valley Chern numbers indicate a nontrivial topology, the minigap is so small as to make it very difficult to meaningfully resolve any real experimental signatures of the finite valley Chern number. Indeed, for practical purposes, when energy resolution is larger than the small minigap $\sim \mu$eV, the minigap cannot be resolved. As a result, the blue and green minibands close to $\tilde{K}, \tilde{K}'$ points resemble Dirac cones with the *same* chirality. This closely mirrors the behavior of the flat minibands in twisted bilayer graphene close to magic angle, where electrons close to $\tilde{K}, \tilde{K}'$ in the moiré Brillioiun zone are severely slowed, and possess the same chirality. The main difference between the green and blue bands in PDS scheme using TMDs is a reduced degeneracy (only two for spin).

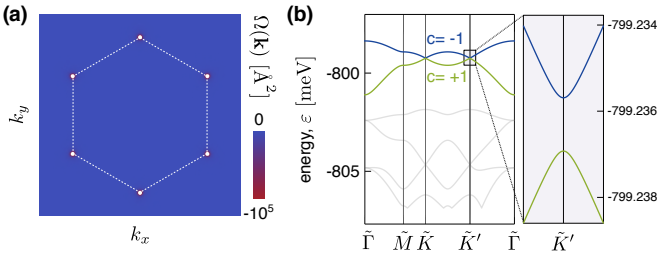

FIG. S-4: Similar to Fig. S-3, but with $V_s = -1.5$ meV with Berry curvature distribution shown for the blue band. Here Berry curvature distribution is sharply peaked close to the corners of the MBZ at $\tilde{K}, \tilde{K}'$ points [clipped white spots denote $|\Omega(\mathbf{k})| > 10^5$ Å^2]. Berry curvature values close to the $\tilde{K}, \tilde{K}'$ points are the same sign indicating the pseudospin winding of the same chirality. Berry curvature about $\tilde{K}, \tilde{K}'$ points both have a negative sign. The panel on the right hand side in (b) shows the tiny gap between two nearly degenerate minibands.

PDS induced minigaps

In this section we discuss how the minigaps between the bundles of flatbands evolve as a function of applied superlattice potential V_s. Here we show the first minigap between minibands in the valence band (i.e., the gap between blue and green bands when $V_s > 0$, and the gap between green and purple band when $V_s < 0$, see Fig. 2 in the main text) as a function of V_s. This indicates that the minigaps increase as larger superlattice potential is applied.

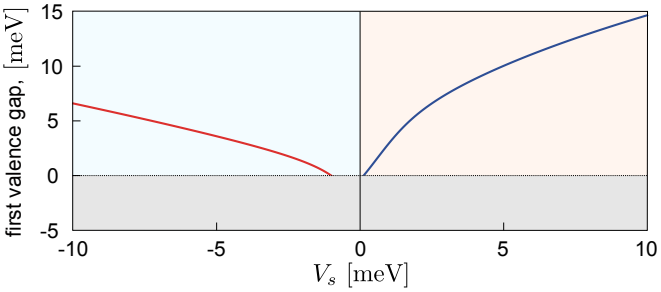

FIG. S-5: PDS induced minigaps between blue and green minibands in the valence band (for $V_s > 0$) as well as between green and purple minibands (for $V_s < 0$). The gray shaded area indicates the region where the minibands are not well separated.

Other types of superlattices

Here we show that square and hexagonal superlattices can also lead to flat bands. For the square superlattice, we follow Ref. [23] and use the superlattice potential

$$V_{\rm squ}(\mathbf{r}) = 2V_s\sigma_0[\cos(\mathbf{b}_1\cdot\mathbf{r})+\cos(\mathbf{b}_2\cdot\mathbf{r})+\cos(\mathbf{b}_1\cdot\mathbf{r})\cos(\mathbf{b}_2\cdot\mathbf{r})], \tag{S-8}$$

where $\mathbf{b}_1 = (2\pi/a)(1,0)$ and $b_2 = (2\pi/a)(0,1)$ with a the superlattice spacing. For hexagonal superlattice, we use the superlattice potential

$$V_{\rm hex}(\mathbf{r}) = V_s\sigma_0 \sum_{j=1,2,3} \big[\cos(\mathbf{G}_i\cdot\mathbf{r}) + \cos(\mathbf{G}_i\cdot\mathbf{r}')\big], \quad \text{(S-9)}$$

where $\mathbf{r}' = \mathbf{r} + (a,0)$, and $\mathbf{G}_j$ are the same reciprocal vectors defined in Eq. S-2 which also apply to hexagonal lattices. The reconstructed minibands are shown in Figs. S-6 and S-7, respectively. These display that flat minibands are also obtained for these superlattices underscoring the generic nature of the PDS flatband scheme.

Other types of TMDs

Here we discuss the PDS scheme (using triangular lattice as illustration) as applied to other types of TMDs, specifically, MoS_2, $MoSe_2$, and WS_2. The results are displayed in Fig. S-8. Here we only show the valence band widths, since the miniband structure possess a symmetry when $V_s \to -V_s$ and $\varepsilon_{\mathbf{k}} \to -\varepsilon_{\mathbf{k}}$ are interchanged (see the above section, "Particle-hole asymmetry"). As expected, flat minibands can be readily achieved.

Estimate for disorder broadening Γ

In this section, we estimate the disorder broadening. We begin by observing that charged impurity scattering is responsible for most of the observed bulk diffusive transport behaviors at low temperature (the contribution of phonons is frozen out). They reside either inside the substrate, or can be desposited near the interface between the substrate and the 2D system during the processing/sample preparation. Here we first extract the impurity concentration $n_{\rm imp}$ from transport measurement results, and then use $n_{\rm imp}$ to estimate the disorder broadening.

We will concentrate on modeling bare WSe_2, where recent low temperature transport measurements have revealed large mobilities $\mu = 3\times10^4\ \mathrm{cm^2\,V^{-1}\,s^{-1}}$ at $T = 1.4\,\mathrm{K}$ for carrier density $n = 2\times10^{12}\ \mathrm{cm^{-2}}$ [24]. To proceed, we first note that close to the band edge of a TMD, the dispersion can be written as $\varepsilon_q = \sqrt{v^2\hbar^2q^2+\Delta^2}$ with $v\hbar = 3.94\,\mathrm{eV\,\AA}$ and $\Delta = 0.8$ eV [27]. For small q, we adopt an effective mass approximation $\varepsilon_q \approx \Delta + v^2\hbar^2q^2/2\Delta$. This produces

$$m^* = \Delta/v^2 = 0.39\,m_e, \quad \text{(S-10)}$$

which is consistent with values obtained in the literature [S1,S2]. Also, within the effective mass approximation, its Fermi wave vector is

$$q_f = \sqrt{\pi n} = 0.25\,\mathrm{nm^{-1}}, \quad \text{(S-11)}$$

where we used $n = 2\times10^{12}\ \mathrm{cm^{-2}}$ [24].

In order to extract an estimate for the impurity density from the mobility, we write the conductivity as

$$\sigma = en\mu = e^2n\tau/m^*, \quad \text{(S-12)}$$

where n is the carrier density (regardless of spin or valley), μ is the mobility, and τ the scattering time. At low temperature, the impurity scattering time reads as

$$\tau^{-1} = n_{\rm imp}\int \mathrm{d}z\,\langle w(\phi_i)(1-\cos\phi_i)\rangle_z, \quad \text{(S-13)}$$

where we assumed an uncorrelated charged impurities $n_{\rm imp}$ (units $\mathrm{cm^{-3}}$) in the substrate, and w is the scattering rate, see below. Eqs. S-12 and S-13 lead to

$$n_{\rm imp} = (e/\mu m^*)\Big[\int \mathrm{d}z\,\langle w(\phi_i)(1-\cos\phi_i)\rangle_z\Big]^{-1}. \quad \text{(S-14)}$$

Within the effective mass approximation,

$$\langle w(\phi_i)(1-\cos\phi_i)\rangle_z = \int \frac{\mathrm{d}\mathbf{q}}{4\pi\hbar}|V(k,z)|^2(1-\cos\theta)\delta(\varepsilon_q-\varepsilon_{q_i}), \quad \text{(S-15)}$$

$$V(q,z) = \frac{2\pi e^2}{\epsilon(q+q_s)}\exp(-qz), \quad \text{(S-16)}$$

where $k = |\mathbf{q}-\mathbf{q}_i|$, $\theta = \phi_{\mathbf{q}} - \phi_{\mathbf{q}_i}$, $\tan\phi_{\mathbf{q}} = q_y/q_x$, $\mathbf{q}_i$ is the initial electron wave vector at the Fermi surface with its magnitude equals to Fermi wave vector q_f, and q_s is the effective screening wave vector.

Eqs. S-14 above enables to estimate $n_{\rm imp}$ from a known mobility. Using this impurity concentration, we can estimate the disorder potential width. To do so, we note that randomly distributed positive and negative charged impurities create fluctuations of the disorder potential. Taking uncorrelated impurity positions, the amplitude of the fluctuations [30–32] is given by

$$\Gamma^2 = \langle[\delta V(\mathbf{r})]^2\rangle = n_{\rm imp}\int \mathrm{d}z\int \frac{\mathrm{d}\mathbf{q}}{(2\pi)^2}V^2(q,z). \quad \text{(S-17)}$$

A numerical estimate for $n_{\rm imp}$ and Γ both require the value for the screening wave vector $q_s = r_s^{-1}$. There are a number of processes that can contribute to screening. For example, at long-wavelengths, Thomas-Fermi screening [S3] yields a screening wavevector as $q_s = (2\pi e^2/\epsilon)\nu_0 = (4e^2/\epsilon)(\Delta/v^2\hbar^2) = 7.4\,\mathrm{nm^{-1}}$, where ν_0 is the density of state at the Fermi energy, and $\epsilon = 4$ for SiO_2. Screening can also arise from a proximal metallic top gate displaced several nanometers away from the vdW layer by $2d$ [17], in this case $q_s \sim d^{-1}$ (assuming a perfect metallic gate). At low densities, non-linear screening can even take effect. The exact value of the disorder potential depends on details of how the Coulomb potential is screened. Instead of identifying the source screening which is beyond the scope of this work, here

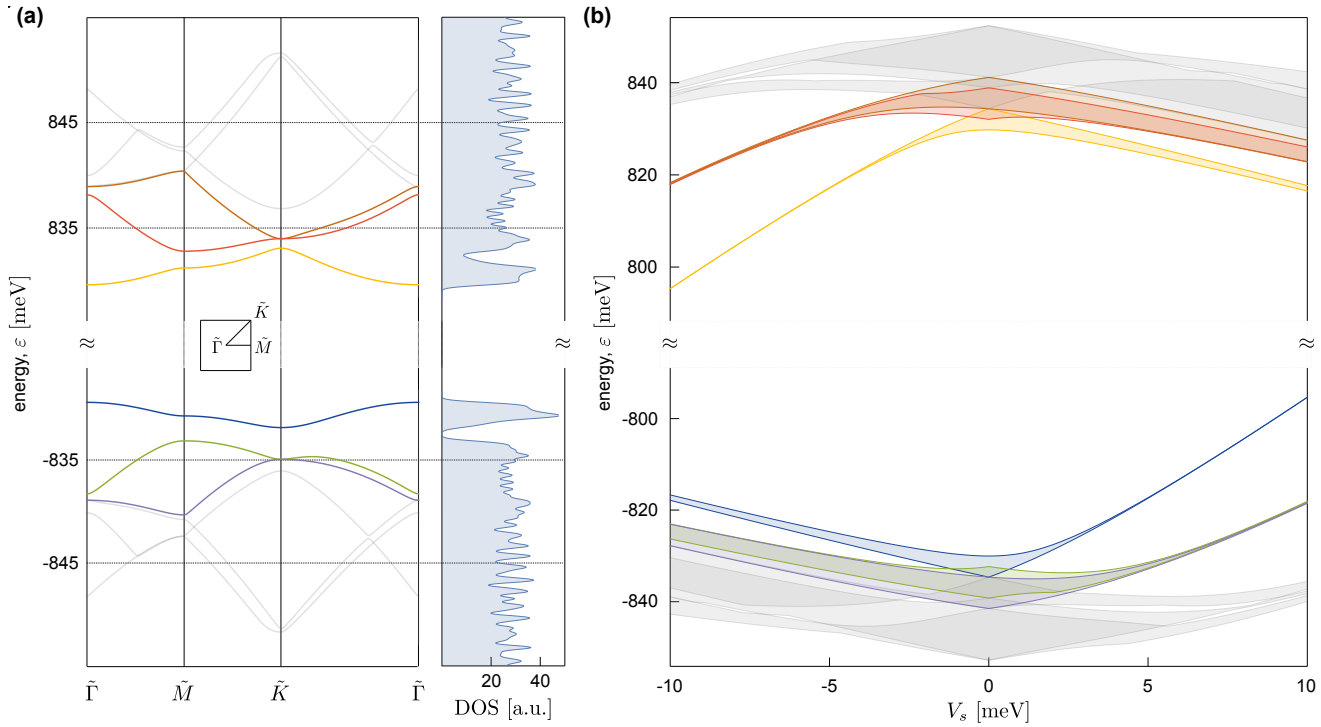

FIG. S-6: Dispersion and DOS at $V_0 = 0.5$ meV (a) and bandwidth (b) for a square superlattice with lattice spacing of 20 nm. Other parameters are the same with those in Fig. 2a in the main text.

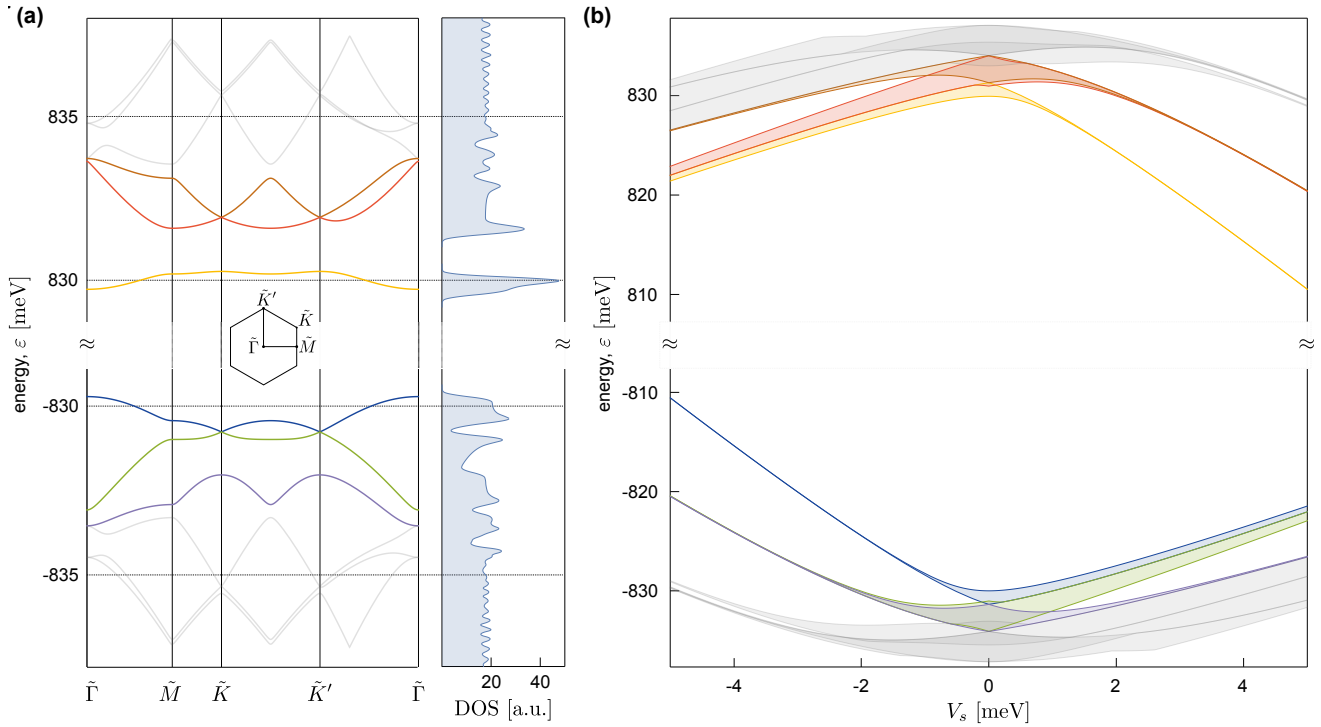

FIG. S-7: Dispersion and DOS at $V_0 = 0.25$ meV (a) and bandwidth (b) for a hexagonal superlattice with inter-hole spacing of 20 nm. Other parameters are the same with those in Fig. 2a in the main text.

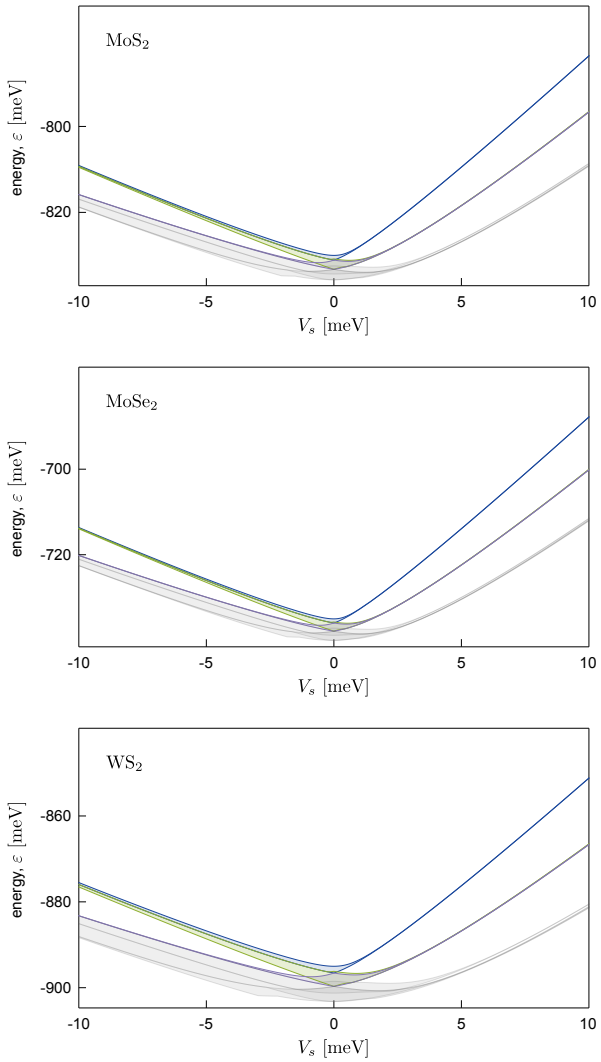

FIG. S-8: Valence miniband widths for triangular PDS for MoS_2 ($v\hbar = 3.51\,\text{eVÅ}$, $\Delta = 0.88\,\text{eV}$), $MoSe_2$ ($v\hbar = 3.11\,\text{eVÅ}$, $\Delta = 0.73\,\text{eV}$), and WS_2 ($v\hbar = 4.38\,\text{eVÅ}$, $\Delta = 0.89\,\text{eV}$). The lattice spacing $a = 20\,\text{nm}$.

we take an *effective* screening wavevector approach. To obtain a rough estimate of the range of values Γ can take on, we plot Γ for a wide range of effective q_s values (Fig. S-9). We find that for ultra-clean WSe_2 samples $\Gamma \sim$ several meV (see Fig. S-9).

We note the above yields an estimate of disorder broadening for bare WSe_2. The precise disorder broadening when the PDS scheme is applied will depend on the details of screening, as well as the actual impurity concentration of the PDS sample. The detailed form as well as the values for these are, at present, unavailable. As a result, the disorder broadening obtained above represents an estimate for the possible disorder broadening in WSe_2 PDS flatbands.

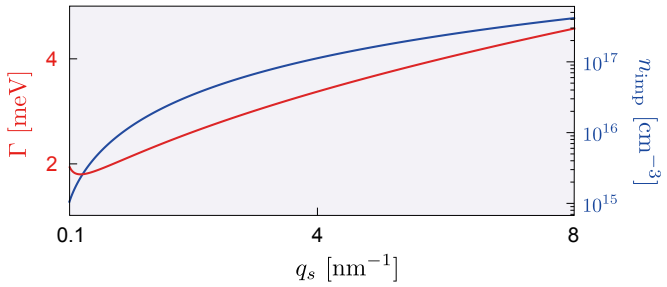

FIG. S-9: Estimated disorder broadening Γ (red) and impurity concentration n_{imp} (blue) for a wide range of effective q_s, for a WSe_2 sample having $n = 2 \times 10^{12}\ \text{cm}^{-2}$ and $\mu = 3 \times 10^4\ \text{cm}^2\,\text{V}^{-1}\,\text{s}^{-1}$ at $T = 1.4\,\text{K}$ recently reported for WSe_2 from the Philip Kim group [24].

Estimate for mean free path ℓ

Here we estimate the mean free path ℓ for the sample which has $n = 2 \times 10^{12}\,\text{cm}^{-2}$, $q_f = \sqrt{\pi n} \approx 0.25\,\text{nm}^{-1}$ and $\mu = 3 \times 10^4\,\text{cm}^2\,\text{V}^{-1}\,\text{s}^{-1}$ [24]:

$$\ell = v_f \tau = \frac{\hbar q_f}{m^*}\frac{\mu m^*}{e} = 0.49\,\mu\text{m}. \tag{S-18}$$

Since $\ell \gg a$, the electronic quasiparticles are able to experience Bragg scattering induced by the PDS superlattice potentials in this sample.

Variational estimate for wavefunction extent a_W

Here we use a variational approach to estimate a_W. We first adopt an effective mass approximation for an electron in conduction band:

$$\hat{H} = -\frac{\hbar^2\nabla^2}{2m^*} + V(\mathbf{r}), \tag{S-19}$$

where $V(\mathbf{r}) = -V_s \sum_{j=1,2,3} 2\cos(\mathbf{G}_j \cdot \mathbf{r})$ is the triangular superlattice potential used in the main text. The minus sign in the potential is to create a local potential minimum for an electron at $\mathbf{r} = \mathbf{0}$.

To proceed in the variational approach, we use a Gaussian trial wave function

$$\psi(\mathbf{r}) = \frac{1}{\sqrt{2\pi a_W^2}} \exp\left(-\frac{\mathbf{r}^2}{4a_W^2}\right), \quad \int d\mathbf{r}[\psi(\mathbf{r})]^2 = 1, \tag{S-20}$$

to describe an electron trapped at $\mathbf{r} = \mathbf{0}$. The energy for this trial wave function is

$$\langle\hat{H}\rangle = \frac{\hbar^2 a_W^{-2}}{4m^*} - 6V_s \exp\left(-\frac{8\pi^2}{9}\frac{a_W^2}{a^2}\right), \tag{S-21}$$

and the equation for its extremum reads as

$$\frac{\partial\langle\hat{H}\rangle}{\partial a_W} = \frac{32\pi^2}{3}\frac{a_W^2}{a^2}V_s \exp\left(-\frac{8\pi^2}{9}\frac{a_W^2}{a^2}\right) - \frac{\hbar^2 a_W^{-2}}{2m} = 0. \tag{S-22}$$

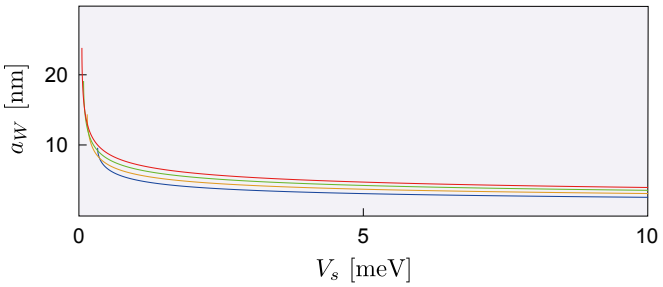

FIG. S-10: Estimate of wavefunction spatial extent a_W (as a function of applied V_s) when confined in a trough of a superlattice. This was obtained using a variational approach and with an effective mass approximation. Blue, yellow, green, and red lines correspond to superlattice wavelengths of $a =$ 20, 30, 40, 50 nm, respectively. For very small V_s, a_w rapidly increases and gets cut off; below this critical V_* the electrons are not well confined in the superlattice troughs.

Eq. S-22 has a finite and positive solution for a_W that decreases with increasing V_s ($\mathbf{e}$ is Euler's number):

$$a_W = \frac{3a}{2\pi}\big[-W_0\big(-\mathbf{e}^{-1}\sqrt{V_*/V_s}\big)\big]^{1/2},\ V_* = \frac{\mathbf{e}^2\pi^2}{54}\frac{\hbar^2 a^{-2}}{2m^*}. \tag{S-23}$$

Here $W_0(z)$ is the the Lambert W function, and $W_0(z)$ only has a real, negative solution when $-\mathbf{e}^{-1} \le z \le 0$. Specifically, $W_0(-\mathbf{e}^{-1}) = -1$ and $W_0(0) = 0$. Therefore, $V_s \ge V_*$ is required for consistency of our initial bound state trial wave function/ansatz, i.e., a finite and positive a_W. When $V_s < V_*$, a_W becomes a complex number, indicating the bound state trial wave function/ansatz fails. As a result, only a large enough $V_s \ge V_*$ is able to trap an electron at its local minimum, and to create a nearly flat band. Thankfully for the TMDs we consider in this work, this critical V_* is small due to their large effective masses (see Fig. S-10). Also, the a^{-2} dependence of V_* shows that larger a makes flatbands easier to achieve at smaller V_s, which is in consistent with what we have shown in Fig. 2b and Fig. 2c in the main text. To illustrate the typical extent of the trapped wavefunction we plot the behavior of a_W versus V_s in Fig. S-10. Here we have used $m^* = 0.39\,m_e$ with $a = 20, 30, 40, 50\,\mathrm{nm}$ corresponding to blue, yellow, green and red lines, respectively. As displayed, even fairly modest values of V_s yield fairly localized a_W.

Flat band ferromagnetism

After discussing how nearly flat bands can be created in TMDs using the PDS scheme, we now demonstrate a possible spontaneous symmetry breaking that arises due the quenching of kinetic energy.

We start from the electronic Hamiltonian

$$H = \sum_{\mathbf{k}\sigma} \xi_{\mathbf{k}\sigma} c^\dagger_{\mathbf{k}\sigma} c_{\mathbf{k}\sigma} + H_{\rm int}, \tag{S-24}$$

where $\xi_{\mathbf{k}\sigma}$ describes the dispersion, and

$$H_{\rm int} = \frac{U}{2\mathcal{V}} \sum_{\mathbf{k}'\mathbf{k}\mathbf{q},\sigma\sigma'} c^\dagger_{\mathbf{k}+\mathbf{q}\sigma} c^\dagger_{\mathbf{k}'-\mathbf{q}\sigma'} c_{\mathbf{k}'\sigma'} c_{\mathbf{k}\sigma}, \tag{S-25}$$

is the electron-electron interaction. Here we only retain the q-independent repulsive interaction U and neglect its large q-dependence, which is strongly suppressed in nearly flat bands [17]. Generally, spin polarization in the z-direction is favored due to repulsive interactions [S4] thus we will focus on the possibility of the spin polarization in the z-direction, and use the mean field parameterization as

$$\langle c^\dagger_{\mathbf{k}\sigma} c_{\mathbf{k}'\sigma'} \rangle = \delta_{\mathbf{k}\mathbf{k}'}\delta_{\sigma\sigma'}\bar{n}_{\mathbf{k}\sigma}. \tag{S-26}$$

Using this meanfield ansatz, we obtain the mean field Hamiltonian

$$H_{\rm MF} = \sum_{\mathbf{k}\sigma} \left(\xi_{\mathbf{k}} + U\bar{n}_{\bar{\sigma}}\right) c^\dagger_{\mathbf{k}\sigma} c_{\mathbf{k}\sigma} - U\mathcal{V}\,\bar{n}_\uparrow \bar{n}_\downarrow, \tag{S-27}$$

where $\bar{\sigma}$ is opposite to σ, and $\bar{n}_\sigma = \mathcal{V}^{-1}\sum_{\mathbf{k}}\langle c^\dagger_{\mathbf{k}\sigma} c_{\mathbf{k}\sigma}\rangle_{\rm MF}$ is the spin σ density with respect to the mean field ground state. For a nearly flat band, we can neglect the $\mathbf{k}$-dependence of $\xi_{\mathbf{k}} \equiv \xi_0$, and its energy density is

$$\langle \bar{H}_{\rm MF}\rangle = \left(\xi_0 + U\bar{n}_\downarrow\right)\bar{n}_\uparrow + \left(\xi_0 + U\bar{n}_\uparrow\right)\bar{n}_\downarrow - U\,\bar{n}_\uparrow\bar{n}_\downarrow, \tag{S-28}$$

where $\langle \bar{H}_{\rm MF}\rangle = \langle H_{\rm MF}\rangle/\mathcal{V}$. In anticipation of the (spin-split) broken symmetry state, we can re-write $\langle \bar{H}_{\rm MF}\rangle$ to emphasize that the Fock exchange interaction favors aligned spins:

$$\langle \bar{H}_{\rm MF}\rangle = \sum_\sigma \left(\varepsilon_0 \bar{n}_\sigma - \frac{U}{2}\bar{n}_\sigma^2\right), \tag{S-29}$$

where $\varepsilon_0 = \xi_0 + U(\bar{n}_\uparrow + \bar{n}_\downarrow)$.

When there is a finite bandwidth Γ [for e.g., arising from disorder broadening (see main text and above)], ε_0 no longer resides at a single flat energy, but instead fluctuates. To capture this, the [single-particle] energy density can be described by a broadened spectral function. Here we have used a simple spectral function $Z(\varepsilon) = A\exp[-(\varepsilon-\varepsilon_0)^2/2\Gamma^2]$ to model this level broadening, where $A = [\sqrt{2\pi\Gamma^2}]^{-1}$. Other choices of spectral function do not modify the qualitative conclusions we describe below and in the main text. As a result, the energy density can be described in close analogy with that used for the energy density in Landau levels [29].

Using the spectral function above, we find the energy density (including disorder broadening) can be modeled as

$$\langle \bar{H}_{\rm MF}\rangle = \sum_\sigma \left[\int^{\mu_\sigma} \mathrm{d}\varepsilon\,\varepsilon Z(\varepsilon) - \frac{U}{2}\bar{n}_\sigma^2\right], \tag{S-30}$$

where μ_σ is the Fermi level for spinor-component σ that satisfies

$$\bar{n}_\sigma = \int^{\mu_\sigma} \mathrm{d}\varepsilon\, Z(\varepsilon). \tag{S-31}$$

As we can see, Eq. S-30 mirrors Eq. S-29 except that the single-particle energy density is now broadened by the spectral function (due to disorder broadening).

In the normal state the two degenerate flat bands are equally occupied. To see whether it is a stable state, we perturb $\bar{n}_\sigma = \bar{n}_0 + \delta\bar{n}_\sigma$ with $\bar{n}_0 = (\bar{n}_\uparrow + \bar{n}_\downarrow)/2$. By using $\sum_\sigma \delta\bar{n}_\sigma = 0$ and expanding $\delta\mu_\sigma$ to the second order, the meanfield energy density reads as

$$\begin{aligned}\langle \bar{H}_{\mathrm{MF}} \rangle = & \sum_\sigma \left[\int^{\mu_0} \mathrm{d}\varepsilon\, \varepsilon Z(\varepsilon) - \frac{U}{2}\bar{n}_0^2 \right] \\ & + \sum_\sigma \frac{\delta\bar{n}_0^2}{2} \left[\frac{1}{Z(\mu_0)} - U \right] + \cdots . \end{aligned} \tag{S-32}$$

From this we see the normal spin-degenerate state is unstable when the second term is negative, i.e., $Z(\mu_0)U > 1$.

* Electronic address: justinsong@ntu.edu.sg

S1. A. Kormányos, G. Burkard, M. Gmitra, J. Fabian, V. Zólyomi, N. D. Drummond, and V. Faíko, 2D Mater. **2**, 022001 (2015).

S2. B. Fallahazad, H. C. P. Movva, K. Kim, S. Larentis, T. Taniguchi, K. Watanabe, S. K. Banerjee, E. Tutuc, Phys. Rev. Lett. **116**, 086601 (2016).

S3. S. Das Sarma, S. Adam, E. H. Hwang, E. Rossi, Rev. Mod. Phys. **83**, 407 (2011).

S4. Y.-H. Zhang, D. Mao, Y. Cao, P. Jarillo-Herrero, T. Senthil, Phys. Rev. B **99**, 075127 (2019).